

## A Frequency Band Reconfigurable UWB Antenna for High Gain Applications

Ritesh K. Saraswat<sup>1, \*</sup> and Mithilesh Kumar<sup>2</sup>

**Abstract**—An octagonal shape patch antenna with switchable inverted L-shaped slotted ground is designed for frequency band reconfigurable and experimentally validated. The antenna is capable of frequency band switching at five different states including an ultra wideband (UWB) state, two narrowband states and a dual-band state by using RF switching element p-i-n diodes. In the case of ultrawide band (UWB) state, the proposed antenna operates over impedance bandwidth of 141% (2.87–16.56 GHz) under simulation and 139% (2.85–15.85 GHz) in measurement with return loss  $S_{11} < -10$  dB. For two narrowband states, 10 dB impedance bandwidth achieved is 16% (5.05–5.91 GHz) and 11% (8.76–9.80 GHz) under simulation and 14% (5.01–5.79 GHz) and 10% (8.68–9.69 GHz) in measurement, respectively. For the dual band state, 10 dB impedance bandwidth of 2.21–2.52 GHz (13%) & 5.07–5.89 GHz (15%) and 2.18–2.52 GHz (14%) & 8.78–9.71 GHz (10%) under simulation and 2.20–2.50 GHz (12%) & 5.05–5.90 GHz (15%) and 2.19–2.50 GHz (13%) & 8.70–9.60 GHz (9%) in measurement with return loss  $S_{11} < -10$  dB. The proposed antenna is capable to serve in different wireless communication applications such as WLAN [802.11b/g/n (2.4–2.48 GHz), 802.11a/h/j/n (5.2 GHz), ISM band (2.4–2.5 GHz)], Bluetooth (2400–2484 MHz), WiMAX (2.3–2.4 & 5.15–5.85 GHz), WiFi (2.40–2.48, 5.15–5.85 GHz) and UWB (3.1–10.6 GHz). It also works at 9.2 GHz where airborne radar applications are found. Next, the antenna gain is improved with the help of a circular loop frequency selective surface (FSS) and a PEC (perfect electric conductor) sheet. Measured peak gain represents average improvements about 4 dB–5 dB over the UWB band. Experimental results seem in good agreement with the simulated ones of the proposed antenna with and without the frequency selective surface.

### 1. INTRODUCTION

In recent years, due to rapid development in the field of wireless communications, the demand with mobile devices operating under different standards or applications is extending. The wireless systems are evolving in the direction of multi-functionality. For multi-functionality, antenna parameters such as operating frequency, radiation pattern, impedance bandwidth and polarization are reconfigured in order to fulfill the current or future demand [1]. Cognitive radio system is one of the future wireless communication systems, where a sensing antenna with the capability of monitoring the spectrum is required, and that can be reconfigured to communicate over a chosen frequency band. In this system, a frequency reconfigurable antenna is required either for spectrum sensing or communication [2]. Most of the frequency-reconfigurable antennas are capable to operate only for narrowband switching modes [3–5]. A switchable quad-band antenna has been proposed by using microelectromechanical systems (MEMS) switch [3]. The microstrip patch antenna can operate in four different frequency modes by controlling the states of switches [4]. Recently, a number of frequency band reconfigurable antennas have been designed, which combine the narrowband and wideband functionalities [6–11]. In [6], a Vivaldi

---

Received 1 September 2015, Accepted 3 November 2015, Scheduled 6 November 2015

\* Corresponding author: Ritesh Kumar Saraswat (ritesh.saraswat9@gmail.com).

<sup>1</sup> M.L.V. Govt. Textile & Engineering College, Bhilwara (Rajasthan), India. <sup>2</sup> Rajasthan Technical University, Kota (Rajasthan), India.

antenna design has been proposed, providing the wideband mode and narrowband mode switching. A frequency band reconfigurable antenna with switching between an ultrawideband (UWB) mode and three narrowband modes has been designed, by using four photoconductive switches [7]. In [9], two reconfigurable monopole antennas are proposed, which provide the combination of narrowband and wideband functionalities, where the first one uses p-i-n diode switches, and the second uses varactor diodes for switching operation. The Field-Effect-Transistor (FET) active switching devices are used in different types of tunable EBG structures where the FET switches are modeled as ideal conductors for determining the transmission of the structure [12]. By changing the electromagnetic bandgaps (EBGs), the bandstop behavior of multistate periodic microwave circuit with very wide stopbands is observed for different states [13].

In this paper, we propose a novel frequency-band reconfigurable antenna with switching facility among UWB, narrowband and dual-band modes. The proposed antenna has five different switchable states: 2.87–16.56 GHz in UWB mode; 5.05–5.91, and 8.76–9.80 GHz in narrowband mode; 2.21–2.52 GHz & 5.07–5.89 GHz and 2.18–2.52 GHz & 8.78–9.71 GHz in dual-band mode. The proposed antenna uses a switchable slotted ground structure for reconfigurability and has a simple structure and the smallest size in comparison to antennas reported in literature [6–11]. To improve the gain of the antenna, a circular loop frequency selective surface is designed and implemented. The FSS is placed beneath the antenna to act as a reflector [14]. The average gain improvement with the FSS antenna combination is around 4 dB. The CST Microwave Studio (CST MWS) software [16] is used for simulation while the measurements are taken using a E5071C (300 kHz–20 GHz) ENA series Agilent Technologies Vector Network Analyzer. The antenna and FSS structure are fabricated with the help of PCB prototype machine Caddo-71. In the following section, the antenna geometry is described in frequency band reconfigurable modes with simulated and measured results. Thereafter, the circular loop FSS and PEC sheet design is described, and the enhancements in the gain and the radiation patterns are discussed. Finally, conclusions are made.

## 2. ULTRAWIDEBAND (UWB) ANTENNA DESIGN

An octagonal shape monopole antenna is chosen as a basic structure to operate over wide bandwidth and has good radiation characteristics. The configuration of the proposed UWB monopole antenna is shown in Figure 1. The antenna is constructed on a Roger RT 5880 substrate with relative permittivity 2.2 and thickness 0.40 mm. The size of the substrate is  $40 \times 40 \text{ mm}^2$ . The radiating element is an octagonal shape patch with dimensions  $ab = ef = 10 \text{ mm}$ ,  $bc = ha = 5.14 \text{ mm}$ ,  $cd = gh = 6.0 \text{ mm}$  and  $de = fg = 5.14 \text{ mm}$ , which is fed with a 50 ohm microstrip feed line with length 22 mm and width 1.25 mm. On the bottom of the substrate, there is a ground plane with  $21.1 \times 40 \text{ mm}^2$  dimensions and height 0.01 mm, below the microstrip feed line.

As per the parametric study of the proposed antenna, variation in the antenna performance with

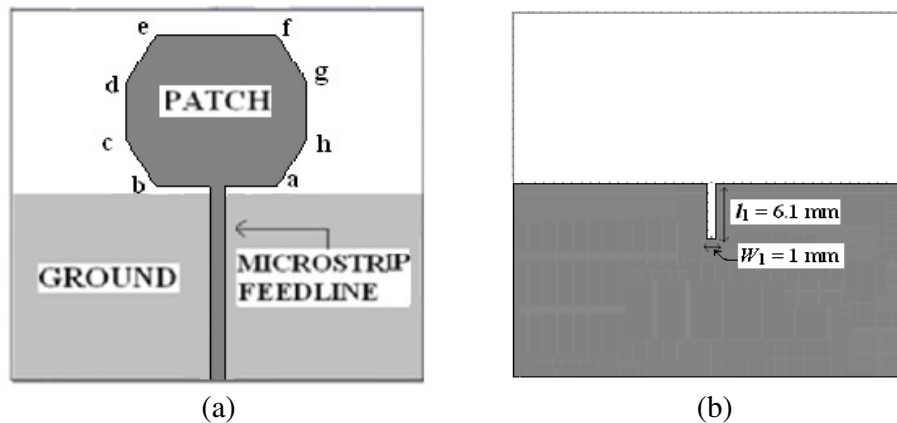


**Figure 1.** Configuration of the UWB antenna. (a) Front view of structure, (b) back view of structure.

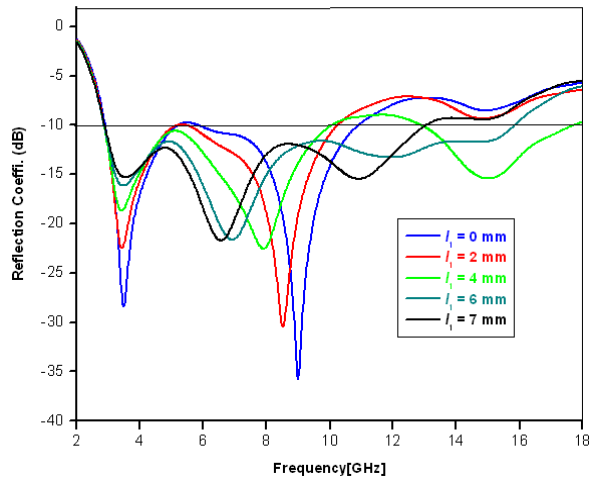


**Figure 2.** Simulated reflection coefficient  $S_{11}$  of the proposed antenna for different values of  $l_1$ .

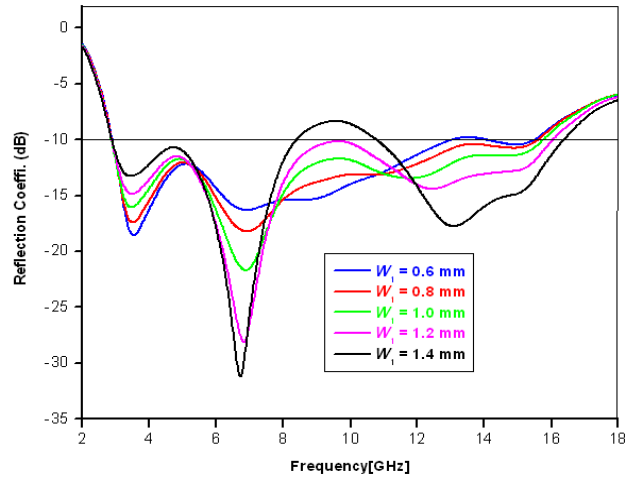


**Figure 3.** Simulated reflection coefficient  $S_{11}$  of the proposed antenna for different values of  $W_1$ .

change in length  $l_1$  and width  $W_1$  of the ground slot is shown in Figures 2–3. As seen, by varying the slot dimensions (length  $l_1$  from 0 to 7 mm and width  $W_1$  from 0.6 to 1.4 mm), the impedance matching with UWB is achieved at length  $l_1 = 6.1$  mm and width  $W_1 = 1$  mm.

It is also observed from Figures 2 and 3 that the impedance matching is improved at lower frequencies (2–4 GHz) when the slot dimensions are reduced (either by reducing  $l_1$  or  $W_1$ ) whereas at higher frequencies (above 5 GHz) it is improved when the slot dimensions are increased.

At the optimized value of  $l_1 = 6.1$  mm and  $W_1 = 1$  mm, the input reflection coefficient  $S_{11}$  of UWB antenna is below  $-10$  dB with impedance bandwidth of 141% (2.87–16.56 GHz) under simulation and 139% (2.85–15.85 GHz) in measurement, shown in Figure 4.

### 3. NARROWBAND AND DUALBAND ANTENNA DESIGN

The UWB monopole antenna can be reconfigured to other frequency bands by using a inverted L and rectangular-shaped slotted structure placed on the ground plane, as shown in Figure 5. This inverted

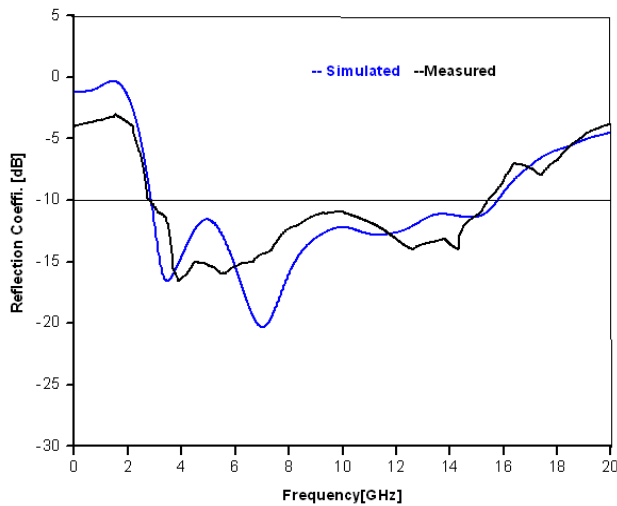


**Figure 4.** Simulated and measured reflection coefficient  $S_{11}$  of the UWB antenna.

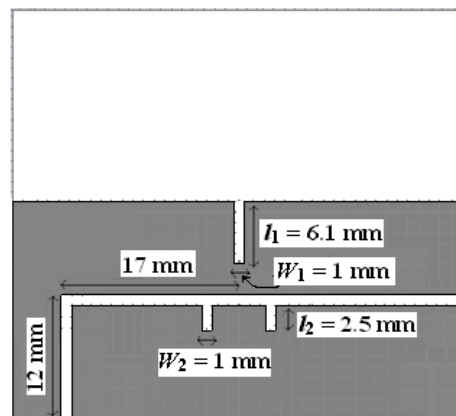


**Figure 5.** Slotted structure on ground plane.

L-slotted structure acts as a filter, which is designed to suppress the frequencies outside the desired frequency band. This embedded slot below the feed line is responsible for stopbands in the UWB range and provides a passband between them [9]. This created passband can be controlled by varying the length and shape of respective slot, as shown in Figure 6.

Figure 7 shows the input reflection coefficient  $S_{11}$  of the antenna below  $-10$  dB for different filter structures. Structures I and II create dual bands whereas structures III and IV are responsible for obtaining the single bands only.

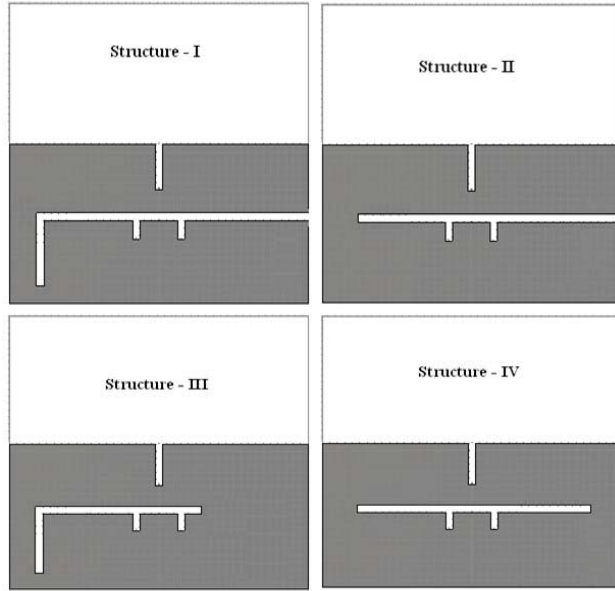


**Figure 6.** Filter structures placed on the ground plane.

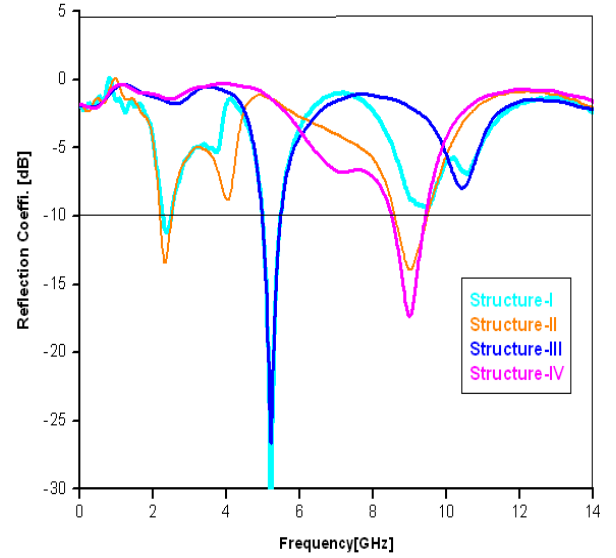


**Figure 7.** Simulated reflection coefficient  $S_{11}$  of the antenna for filter structures in Figure 6.

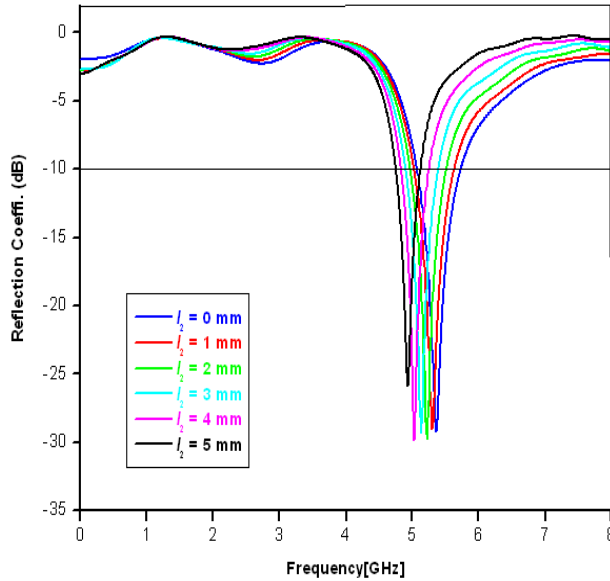


**Figure 8.** Simulated reflection coefficient  $S_{11}$  of the antenna for different values of  $l_2$  in structure-III.

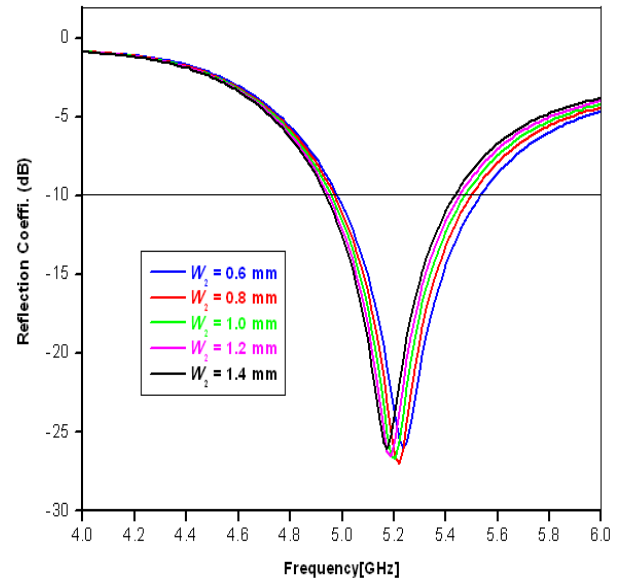


**Figure 9.** Simulated reflection coefficient  $S_{11}$  of the antenna for different values of  $W_2$  in structure-III.

Moreover, the bandwidth of each filtering structure in Figure 7 is controllable with changing the length  $l_2$  and width  $W_2$  of parallel vertical arms (in Figure 5). By the variations of these arms dimensions, impedance bandwidth changes accordingly, as shown in Figures 8–9. By increasing the slot length  $l_2$  and width  $W_2$ , bandwidth of the antenna decreases from 30% to 12% in structure III. Finally, the variations in the impedance bandwidth with changes in the slot dimensions indicate the presence of optimal values for the best performance.

#### 4. RECONFIGURABLE ANTENNA DESIGN

This section is devoted to discussion on the design of an antenna which is capable of reconfiguration from UWB to two narrowband and two dual-band modes by using the filter structure on ground plane and inserting five p-i-n diode switches inside it, as shown in Figure 10. By changing effective length of the slot, different resonant frequency bands can be produced. The switches  $D_1$ – $D_5$  are positioned in such a way to obtain the required structures I–IV for desired frequency bands. If diode  $D_1$  is on and remaining ones are off, we will get a filter structure like structure-I for dual-band.

For switching operation of p-i-n diodes, we apply dc voltage by using metal strips dimension of  $2 \times 0.6 \text{ mm}^2$  inside the main slot, as shown in Figure 10. A 100-pF dc blocking capacitor is also present in the slot, for each p-i-n diode, to provide the RF connection of the p-i-n diode as well as to isolate the RF signal from the dc. In the proposed design, ALPHA-6355 beam lead p-i-n diodes with extremely low capacitance are used [15]. For biasing of p-i-n diodes, a 0.7 V dc voltage is applied to metal strips. The ALPHA-6355 beam lead p-i-n diode exhibits an ohmic resistance of 2.6 ohm and a capacitance of 0.081 pF in the ON (forward bias) and OFF states (reverse bias), respectively. When the diodes are turned on, the metal strips are connected to the ground plane and become a part thereof.

The desired frequency band can be obtained by changing the states of five p-i-n diodes, as per Table 1. The RF equivalent circuit of the p-i-n diode is shown in Figure 11. In the case of ON-state (forward bias), the p-i-n diode works as a current-controlled resistor ( $R_s$ ) connected in series with a fixed inductor ( $L_s$ ). In OFF-state (reverse bias) of p-i-n diode, the equivalent circuit shows a shunt combination of the intrinsic-layer capacitance ( $C_p$ ) and the parallel resistance ( $R_s$ ) in series with the fixed inductance ( $L_s$ ). The depleted intrinsic layer consist capacitive reactance  $C_p$  and the shunt resistance  $R_s$ . The reactive capacitance  $C_p$  contains the stray capacitance  $C_s$  due to the effects of the diode’s package structure and the junction’s capacitance  $C_j$ .

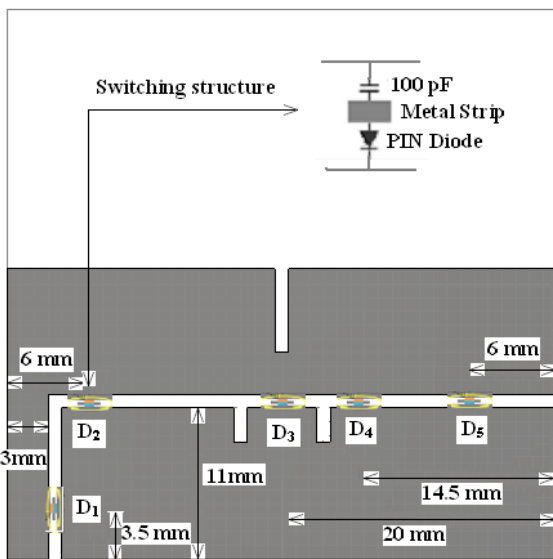


**Figure 10.** Switchable filter structure on the ground plane (unit: millimeters).

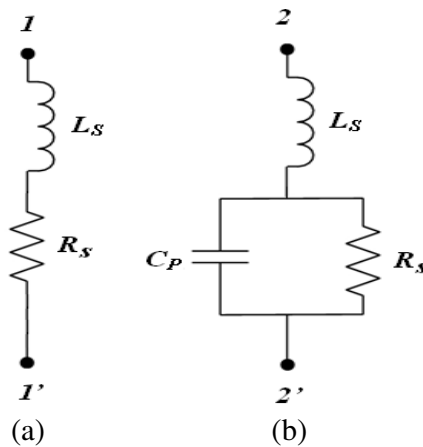


**Figure 11.** Equivalent circuit for p-i-n diode: (a) ON-state (forward bias), (b) OFF-state (reverse bias).

**Table 1.** Details of combinations of p-i-n diodes with simulated and measured frequency band and bandwidth in each states.

Diode → States ↓	D <sub>1</sub>	D <sub>2</sub>	D <sub>3</sub>	D <sub>4</sub>	D <sub>5</sub>	Frequency Bands (in GHz)		10-dB bandwidth (%)		Characteristics
						Simulated	Measured	Simulated	Measured	
I	ON	OFF	OFF	ON	OFF	5.05–5.91	5.01–5.79	16	14	Narrow Band
II	OFF	ON	OFF	OFF	ON	8.76–9.80	8.68–9.69	11	10	Narrow Band
III	ON	OFF	OFF	OFF	OFF	2.21–2.52 & 5.07–5.89	2.20–2.50 & 5.05–5.90	13 & 15	12 & 15	Dual Band
IV	OFF	ON	OFF	OFF	OFF	2.18–2.52 & 8.78–9.71	2.19–2.50 & 8.70–9.60	14 & 10	13 & 9	Dual Band
V	ON	ON	ON	ON	ON	2.87–16.56	2.85–15.85	141	139	UWB

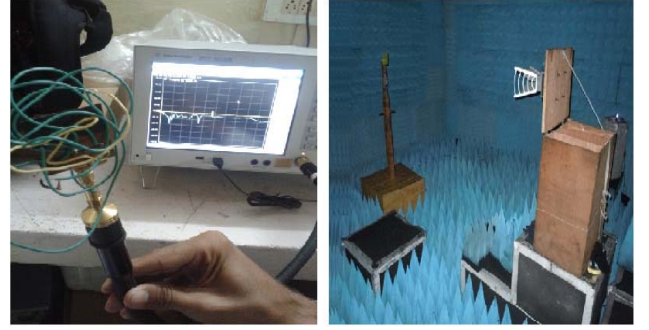
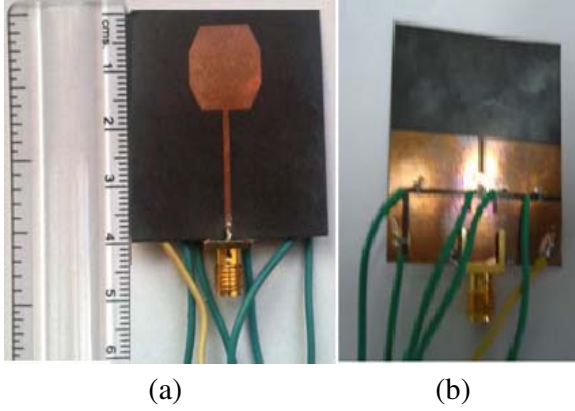


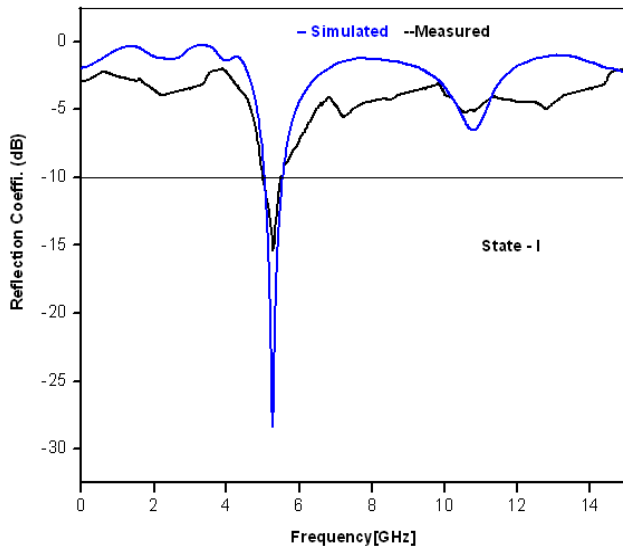
**Figure 12.** Images of the fabricated antenna: (a) top view; (b) bottom view.

**Figure 13.** Images of measurement setup for proposed antenna.

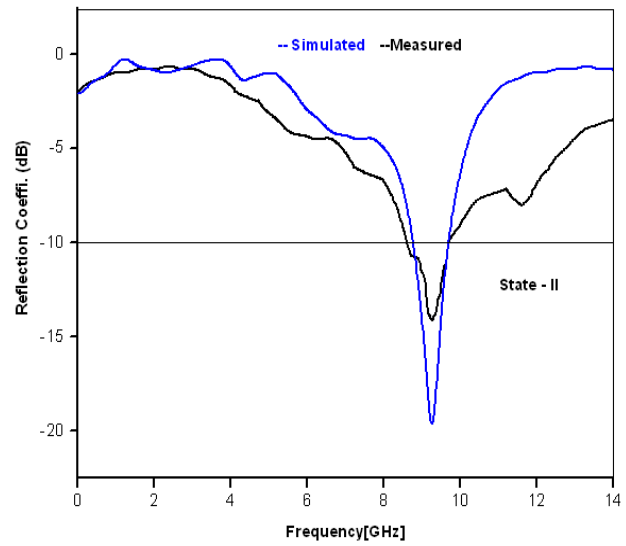
The proposed antenna is initially simulated on CST Microwave Studio (MWS) software [16] and then fabricated with the optimized dimensions, as shown in Figure 12. As per Table 1, the five operating states are investigated, and their corresponding diodes states with comparison of the simulated and measured results of frequency bands and impedance bandwidth. With respect to all the five states, the measured and simulated reflection coefficients  $S_{11}$  are compared as shown in Figures 14–18 which seem to be in good agreement. As per Table 1, for States I and II two narrowband states, 10 dB impedance bandwidth achieved is 16% (5.05–5.91 GHz) and 11% (8.76–9.80 GHz) under simulation whereas 14% (5.01–5.79 GHz) and 10% (8.68–9.69 GHz) in measurement respectively. For States III and IV, the antenna operates in dual bands, impedance bandwidth of 13% (2.21–2.52 GHz) & 15% (5.07–5.89 GHz) and 14% (2.18–2.52 GHz) & 10% (8.78–9.71 GHz) under simulation and 12% (2.20–2.50 GHz) & 15% (5.05–5.90 GHz) and 13% (2.19–2.50 GHz) & 9% (8.70–9.60 GHz) in measurement respectively. For UWB state, the antenna operates over impedance bandwidth of 141% (2.87–16.56 GHz) under simulation and 139% (2.85–15.85 GHz) in measurement with return loss  $S_{11} < -10$  dB.

Figure 13 shows the measurement setup for proposed antenna to obtain the measured reflection coefficient by using vector network analyzer (VNA) and radiation characteristics with the help of anechoic chamber.

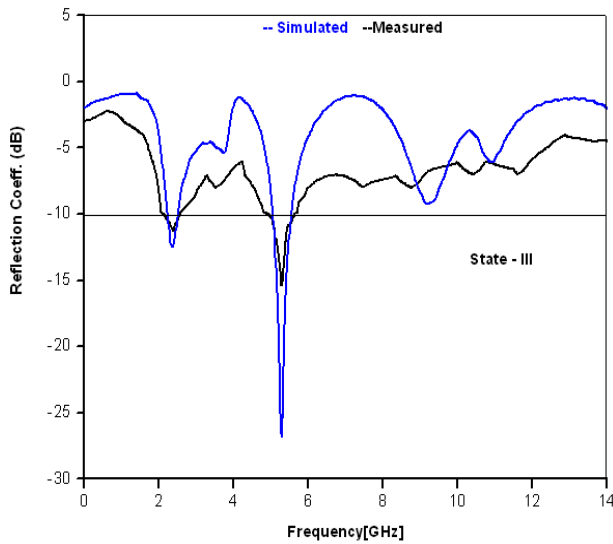
The frequency bandwidth is obtained by switching among different states that can serve several wireless applications, according to 802.11b/g/n (2.4–2.48 GHz), 802.11a/h/j/n (5.2 GHz) and ISM band ranging from 2.4 GHz to 2.5 GHz and are used for different WLAN applications, including the Bluetooth (2400–2484 MHz), WiMAX (2.3–2.4 & 5.15–5.85 GHz), WiFi (2.40–2.48, 5.15–5.85 GHz) and UWB (3.1–10.6 GHz). It is also works at 9.2 GHz where airborne radar applications are found.



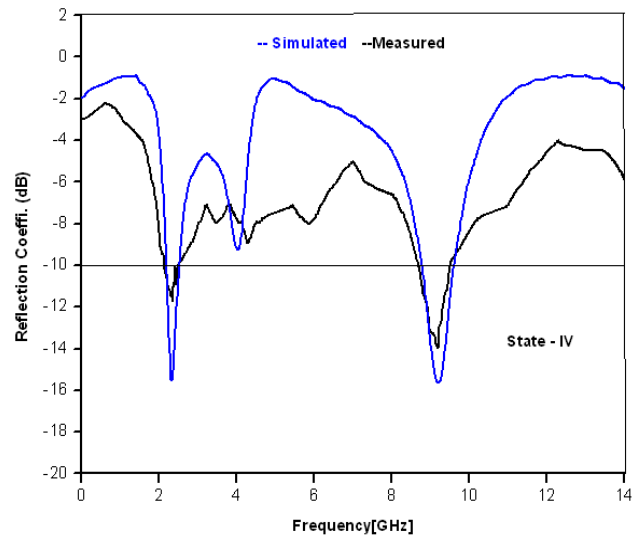
**Figure 14.** Simulated and measured reflection coefficient  $S_{11}$  of the proposed antenna for State-I (from Table 1).



**Figure 15.** Simulated and measured reflection coefficient  $S_{11}$  of the proposed antenna for State-II (from Table 1).



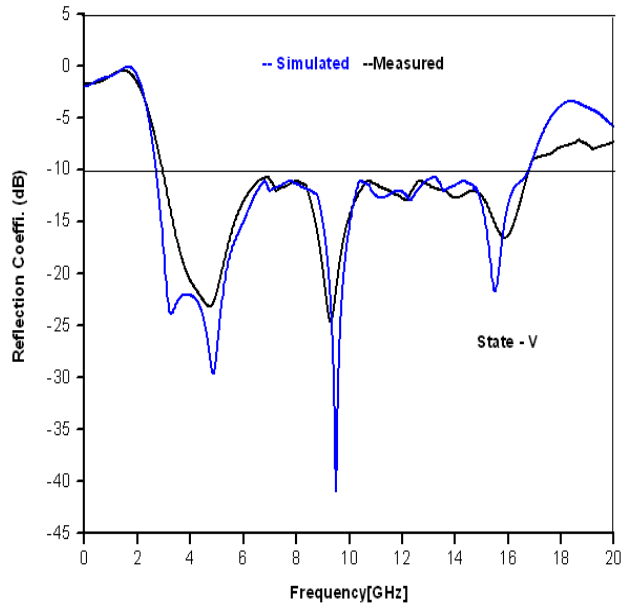
**Figure 16.** Simulated and measured reflection coefficient  $S_{11}$  of the proposed antenna for State-III (from Table 1).



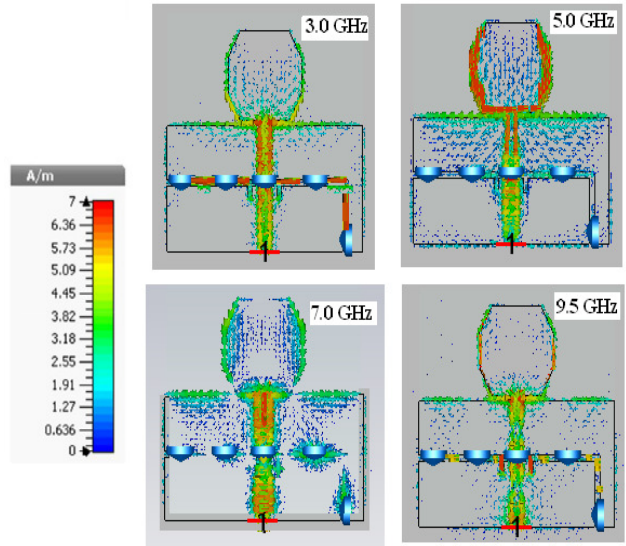
**Figure 17.** Simulated reflection coefficient  $S_{11}$  of the proposed antenna for State-IV (from Table 1).

From the simulated reflection coefficient (blue line, Figure 18), resonance can be noted at 3.0 GHz, 5.0 GHz, 7.0 GHz and 9.5 GHz. The first resonance is controlled by the variation in the dimensions of inverted L-shaped slot. An octagonal shape patch at the end of the CPW line acts as a monopole and results in the resonance at 5.0 GHz. The rectangular slot on the ground plane causes the resonance at 7.0 GHz while the higher resonance at 9.5 GHz seems to originate in the tank circuits formed by two rectangular slits which are attached with the inverted L-shaped slot. A plot of the surface current distribution at these resonances is shown in Figure 19 which justifies the above observations.

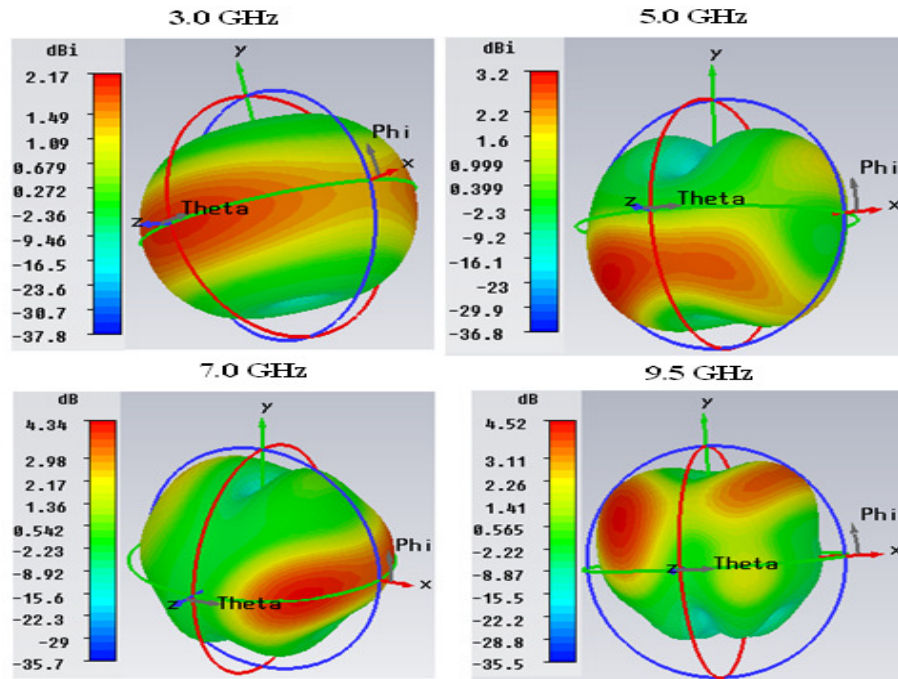




**Figure 18.** Simulated and measured reflection coefficient  $S_{11}$  of the proposed antenna for State-V (from Table 1).



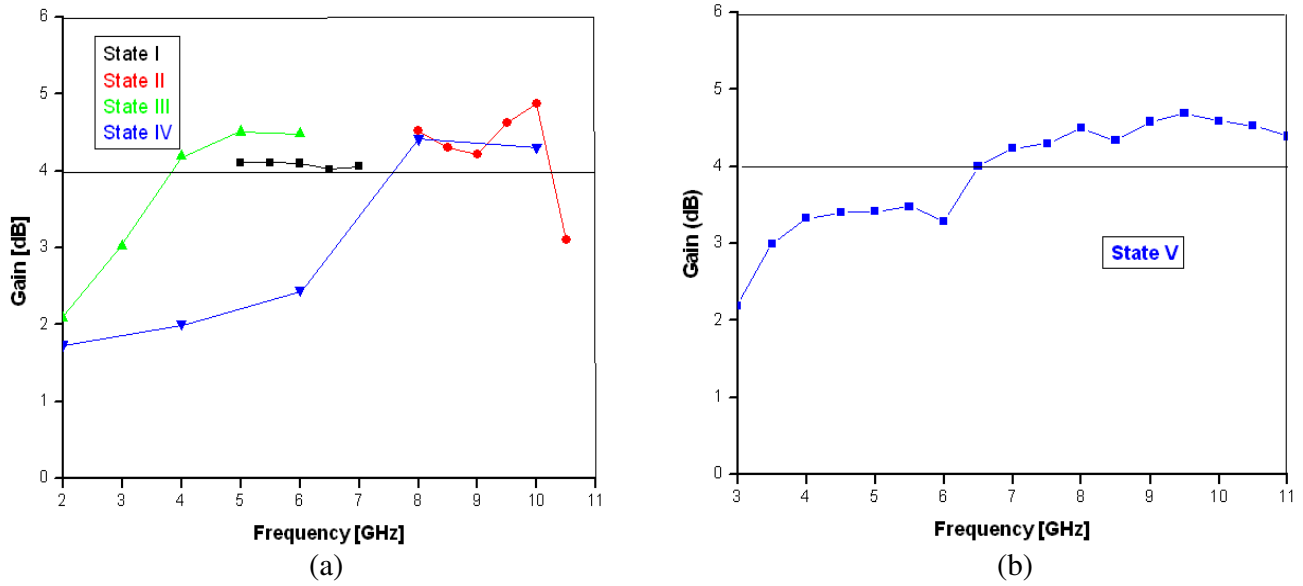
**Figure 19.** Surface current distribution of the proposed antenna for different frequencies.



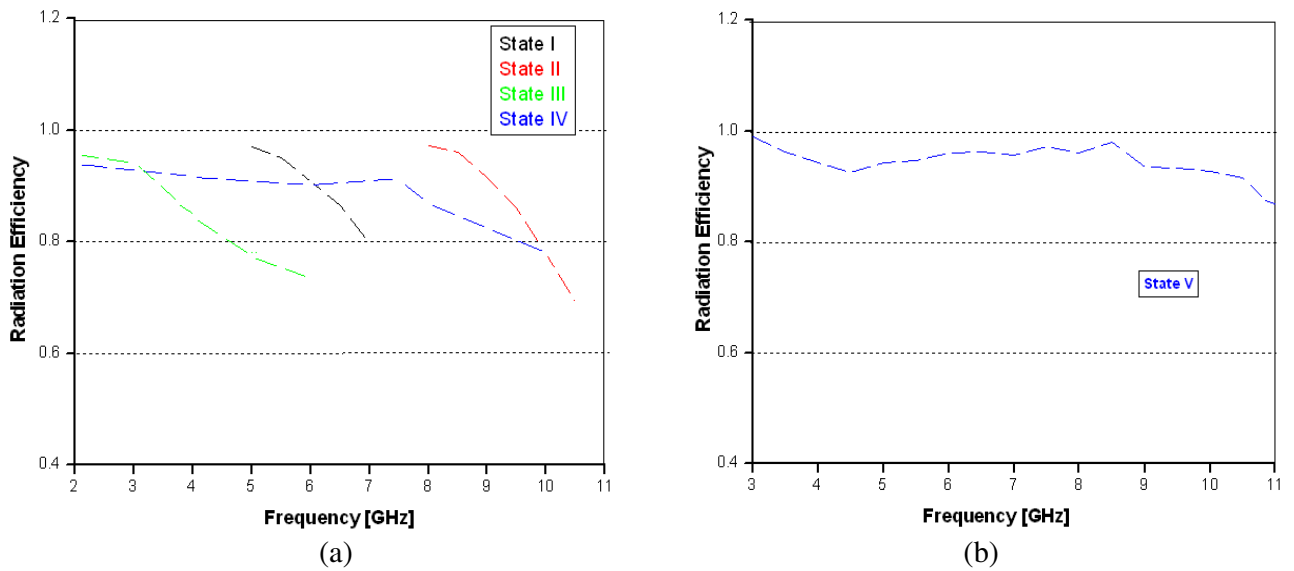
**Figure 20.** Simulated gain (dB) of the proposed antenna for different frequencies.

Figure 20 shows the 3D-gain of the proposed antenna at different resonance frequencies, which indicates the maximum radiation in direction with respect to different values of theta and phi. At higher resonant frequency, directivity is increased so that gain is improved. The measured antenna gain in different states is exhibited in Figure 21. At lower frequencies (below 6 GHz), the gain is less than the





**Figure 21.** Measured gain of the proposed antenna for different switching states: (a) single-band and dual-band modes, (b) UWB.



**Figure 22.** Simulated radiation efficiency of the proposed antenna for different switching states: (a) single-band and dual-band modes, (b) UWB.

reference level of 4 dB whereas at higher frequencies (above 6 GHz), the gain is improved with respect to the reference level. The antenna has an acceptable gain in narrowband and dual-band modes and a reasonably flat gain with an average of 3.9 dB in UWB mode.

As per Figure 22(a), in the case of States I and II for the proposed reconfigurable antenna, the simulated radiation efficiency varies from 96.9% to 79.5% and from 97.2% to 70.3%, respectively. For States III and IV, the simulated radiation efficiency changes from 95.5% to 73.3% and from 94.0% to 78.1%, respectively. From Figure 22(b), in the case of State V for UWB mode, efficiency varies from 98.9% to 85.8%. So it is observed that the efficiency stays above 70% in all the operating band, and as the frequency increases, the radiation efficiency decreases.

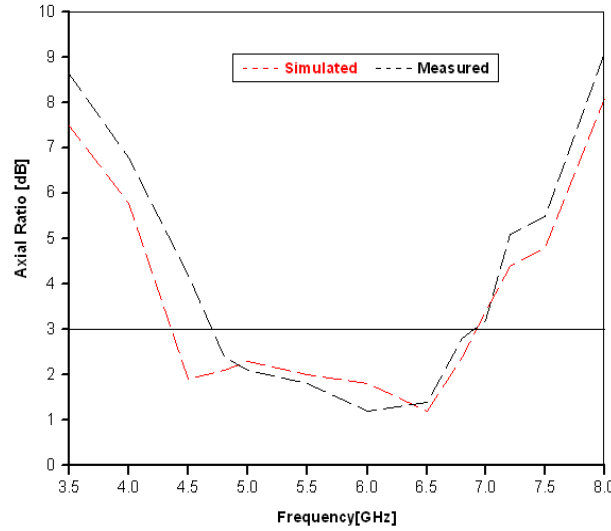


**Figure 23.** Simulated and Measured AR (axial ratio) (along  $\theta = 78^\circ$  and  $\Phi = -89^\circ$ ) of the proposed antenna.

The axial ratio (AR) of the proposed antenna is measured with the help of Antenna Measurement System in conjunction with a Vector Network Analyzer inside an anechoic chamber. For obtaining the best performance regarding maximum ARBW (Axial ratio bandwidth) as shown in Figure 23, the measurement system is set up along the directions of  $\theta = 78^\circ$  and  $\Phi = -89^\circ$ . The simulated AR stays less than 3 dB from 4.4–6.9 GHz which represents an ARBW of 44% centered at 5.65 GHz. The measured ARBW (axial ratio bandwidth) is slightly less than the simulated ARBW at 38% (4.65–6.85 GHz) as shown in Figure 23. The wideband CP is achieved by optimizing the inverted L-shaped slot and rectangular slit on ground plane. Inverted L-shaped slot on the ground plane creates alternate current paths that produces two orthogonal degenerate modes on the top patch whereas the CP behavior can be enhanced by creating rectangular slits in ground plane.

## 5. CIRCULAR LOOP FSS DESIGN FOR GAIN ENHANCEMENT

An FSS of  $8 \times 8$  circular loop is designed to improve the gain of the proposed antenna. The FSS is formed by a metallic PEC sheet with circular loop of diameter  $D = 7$  mm on both sides of an FR4 substrate of relative permittivity  $\epsilon_r = 4.4$  and thickness 1.6 mm. A schematic of the FSS is shown in Figure 24.

The circular loop of diameter 7 mm is considered as a square loop of side length 6.2 mm [17]. The relation between the area of square loop and area of circular loop is shown in Equation (1).

$$l \times l = \pi r^2, \quad (1)$$

where,  $l$  is the side length of square loop and  $r$  the radius of circular loop.

As per Figure 25 and Equation (1), circular loop unit cell dimension ( $d_u$ ) is corresponding to twice of the side length of the square loop.

As shown in Figure 24, circular loop type FSS combines the characteristics of the patch type FSS and slot type FSS and is chosen for its broad band operation. In the comparison of the transmittance with a single layer circular loop FSS to a double layer circular loop FSS in Figures 26 and 27, it is easily seen that a wider bandwidth of 6.7 GHz (3.5–10.2 GHz) is achieved in the case of the latter. The impedance bandwidth so obtained is near UWB bandwidth 7.5 GHz (3.1–10.6 GHz).

An equivalent circuit for the square loop FSS is proposed in [18], and for circular loop FSS, an equivalent circuit is represented with the substrate of characteristic impedance  $Z_{\text{sub}}$  and lumped inductance and capacitance in series, as shown in Figure 28, where  $Z_0$  is the characteristic impedance of air. The values of lumped inductance  $L$  and capacitance  $C$  can be computed by using following

Equations (2) & (3) [19, 20].

$$\omega L = (d_u/p)F(p, 2w_m, \lambda) \tag{2}$$

$$\omega C = 4\epsilon_r(d_u/p)F(p, g_a, \lambda) \tag{3}$$

where,  $F(p, 2w_m, \lambda) = (p/\lambda)[\ln\{\operatorname{cosec}(\pi \cdot 2w_m/2p) + G(p, w_m, \lambda)\}]$  and  $F(p, g_a, \lambda) = (p/\lambda)[\ln\{\operatorname{cosec}(\pi \cdot g_a/2p) + G(p, g_a, \lambda)\}]$ .

The characteristics of the proposed circular loop FSS are measured in an anechoic chamber. For measurement, two double ridge horn antennas are used as reference antennas. Figure 29 shows the block diagram of the used measurement setup. The proposed FSS is placed between the two horn antennas (reference antennas) so that it is in the far-field region of both the antennas. The FSS is illuminated by the plane waves generated by the transmitting horn antenna at the transmitter section, and the transmitted waves through the FSS are collected by the receiving horn antenna at the receiver section. The ratio of received signal strength to transmitted signal strength ( $S_{21}$ ) is calculated using Vector Network Analyzer (VNA).

From Equations (2) and (3),  $\omega L$  is the inductive reactance associated with inductance  $L$ , and  $\omega C$  is the capacitive susceptance associated with capacitance  $C$ .  $G$  is the correction factor for the associated

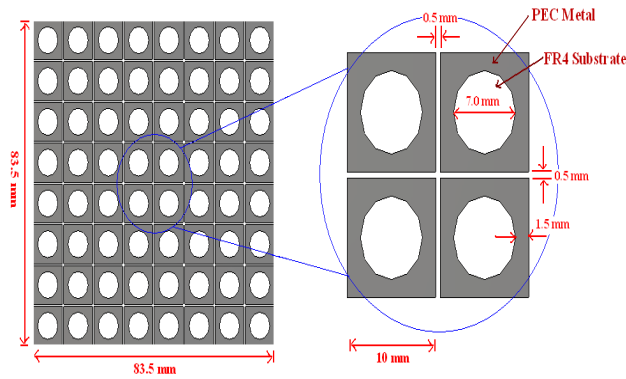


**Figure 24.** Schematic of the proposed FSS with dimensions of the unit cell and periodicity.

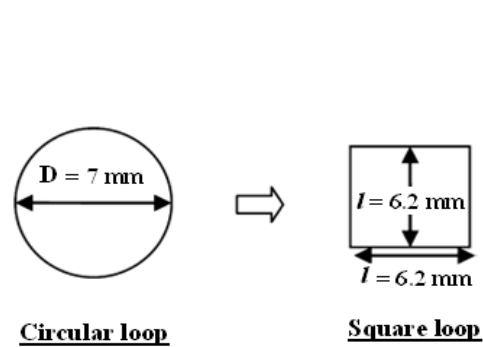


**Figure 25.** Schematic diagram for equating the area of square loop with circular loop.

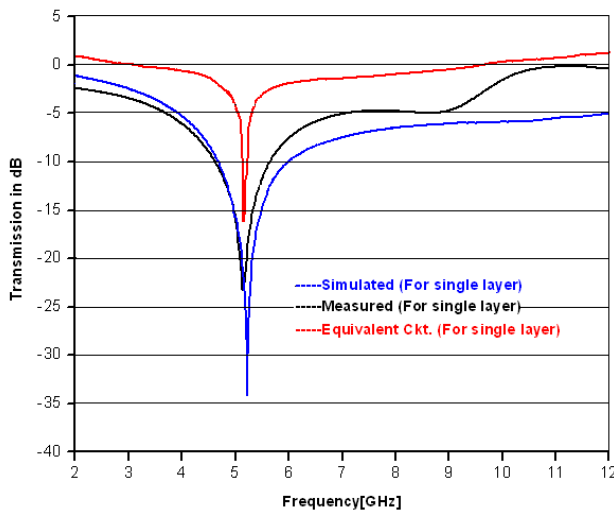


**Figure 26.** Simulated and measured transmission (in dB) for the circular loop FSS for single layer.

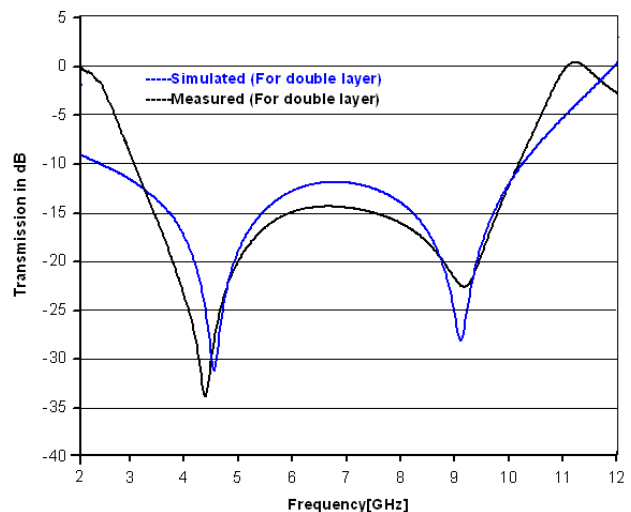


**Figure 27.** Simulated and measured transmission (in dB) for the circular loop FSS for double layer.

inductance and capacitance and can cause minor deviation in the results if it is ignored in the present calculations. The admittance of the shunt branch representing the FSS may be expressed as,

$$Y = \{j\omega L + (1/j\omega C)\}^{-1} \quad (4)$$

and the magnitude of the transmission coefficient  $|\tau|$  for a single FSS layer is obtained by,

$$|\tau|^2 = [4 / \{4 + |Y|^2\}] \quad (5)$$

The resonance frequency can be determined by applying the condition,

$$\omega L = (1/\omega C) \quad (6)$$

For a circular loop FSS layer with dimensions as given in Table 2 and with  $\epsilon_r = 2.7$  (the mean of air and FR4), the calculated value of inductive reactance  $\omega L$  is  $10.3537\lambda^{-1}$ , and capacitive susceptance  $\omega C$  is  $347.3714\lambda^{-1}$ . With these values of  $\omega L$  and  $\omega C$  and with the help of Equation (6), the calculated resonance comes out to be 5.01 GHz. Also, the transmission coefficient magnitude  $|\tau|$  is calculated by using Equations (4) and (5).

**Table 2.** Dimensions of the circular loop FSS.

Parameter	Value (in mm)
Periodicity ( $p$ )	10.5
Gap ( $g_a$ )	0.5
Width of metallic loop ( $w_m$ )	1.5
Dimension of the unit cell ( $d_u$ )	12.4

The size of FSS layer and distance from the antenna are optimized as per Tables 3(a) & (b), respectively.

The distance from the antenna at which the proposed FSS is to be placed is also decided from the reflection phase behavior. The distance should allow for constructive interference between the radiation from antenna and the reflected radiation from the FSS screen. In order to meet the requirement, we use a simple expression which can be written as given in Equation (7).

$$\Phi_{\text{FSS}} - 2\beta h_d = 2n\pi \quad (7)$$

where,  $n = \dots, -2, -1, 0, 1, 2, \dots$

$\Phi_{\text{FSS}}$  is the reflection phase of the FSS screen,  $h_d$  the distance at which the FSS is to be placed from antenna, and  $\beta$  the propagation constant of free space given by  $2\pi/\lambda$ . If we choose the reflection phase  $\Phi_{\text{FSS}}$  to be  $0^\circ$ , the optimal height can be shown to be  $h_d = \lambda/2$ . Hence, the optimal height ( $h_d$ ) can be taken equal to half the wave-length ( $\lambda/2$ ) at that frequency where the reflection phase of the

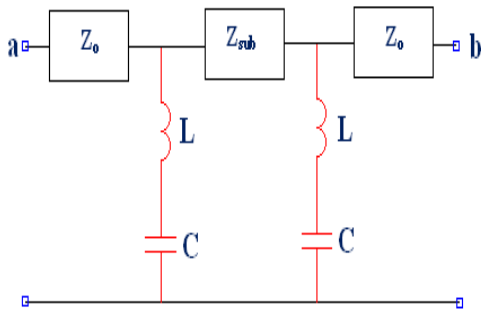


**Figure 28.** Equivalent circuit for the circular loop FSS.

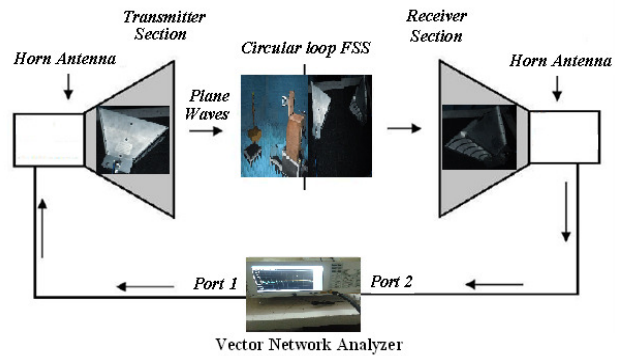


**Figure 29.** Block diagram of measurement setup [20].

**Table 3.** Size and distance optimization for FSS.

(a) Size optimization for the FSS.

Size of FSS Sheet (in mm <sup>2</sup> )	Distance of FSS from antenna Structure (in mm)	Peak Gain (in dB)
40 × 40	20	5.47
60 × 60	20	6.7
80 × 80	20	8.31
83.5 × 83.5	20	8.57
100 × 100	20	8.47
120 × 120	20	8.53

(b) Distance optimization for the FSS.

Size of FSS Sheet (in mm <sup>2</sup> )	Distance of FSS from antenna Structure (in mm)	Peak Gain (in dB)
83.5 × 83.5	05	7.76
83.5 × 83.5	10	8.24
83.5 × 83.5	15	8.29
83.5 × 83.5	20	8.57
83.5 × 83.5	25	8.26
83.5 × 83.5	30	7.45

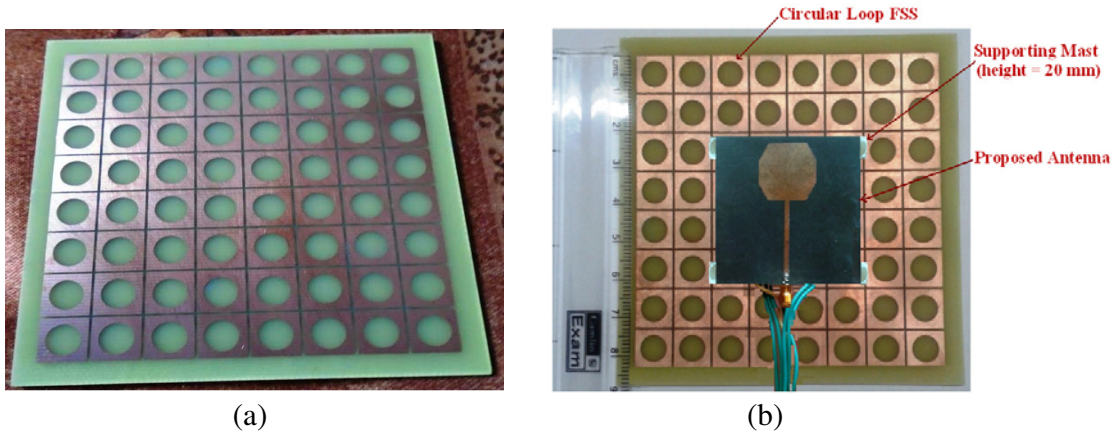


**Figure 30.** (a) Image of proposed FSS without structure (side view), (b) image of proposed FSS with structure (top view).

FSS ( $\Phi_{FSS}$ ) is zero. For the designed circular loop FSS, the frequency at which the reflection phase is  $0^\circ$  is found to be 7.51 GHz. Hence, the optimal height is calculated as 20 mm. In Figure 30, an image of the circular loop FSS screen is shown while the antenna along with the FSS screen is mounted at optimal height of 20 mm.

A comparison of simulated and measured reflection coefficients ( $S_{11}$ ) of the antenna without the FSS and with the circular loop FSS are shown in Figure 31. It can be seen from Figure 31 that the impedance bandwidth more or less remains the same after the application of the FSS screen. The impedance matching slightly deteriorates in the presence of the FSS due to induced current from reflected radiation with varying phase at other frequencies.

The measured and simulated radiation patterns of the proposed antenna with and without FSS are shown in Figure 32. The radiation patterns are plotted for selected frequencies in the two principal planes  $E$ -plane and  $H$ -plane. From Figure 32, it is seen that the  $E$ -plane ( $XZ$  plane) patterns are quasi-

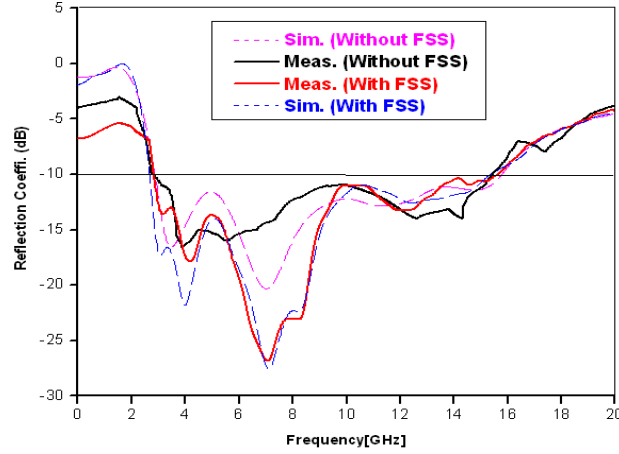


Figure 31. Comparison of simulated and measured reflection coefficients without and with the FSS.

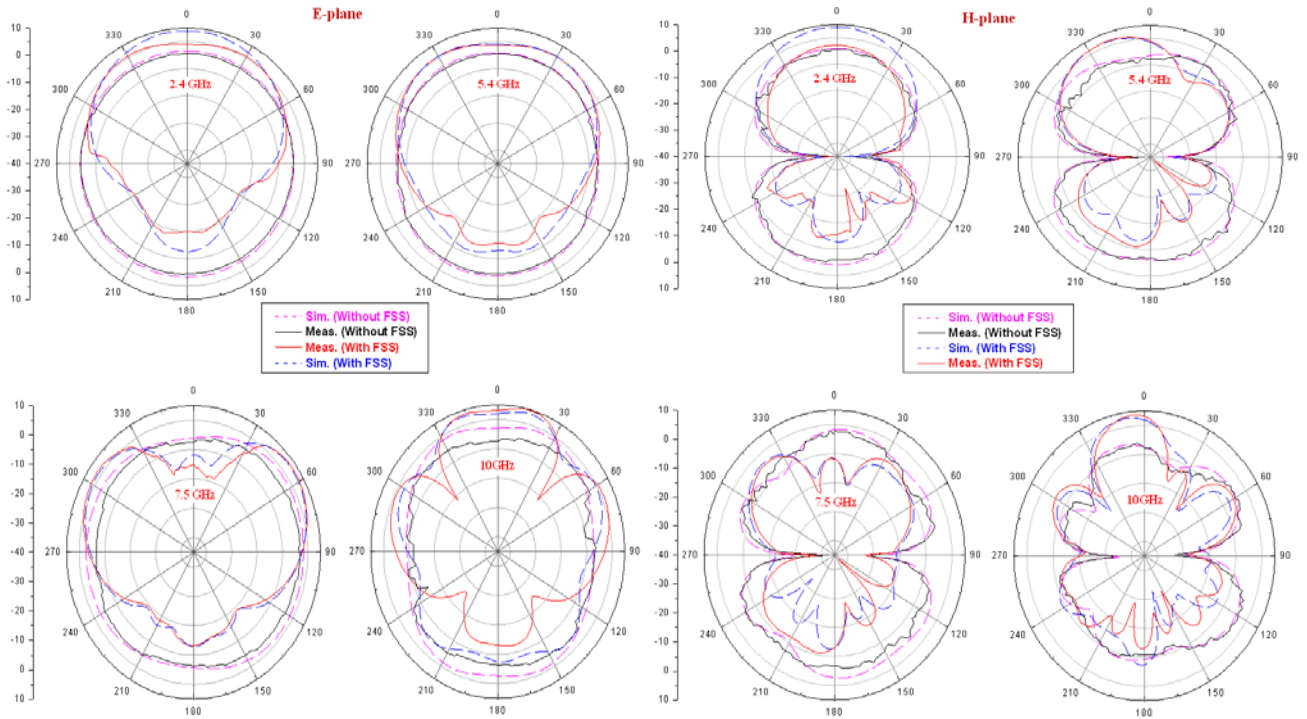
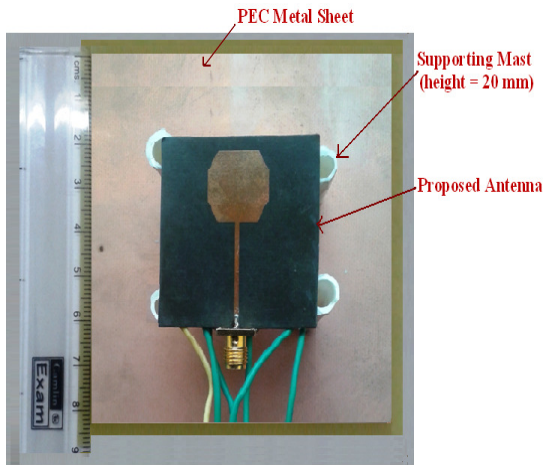


Figure 32. Measured and simulated radiation patterns (antenna with and without FSS).

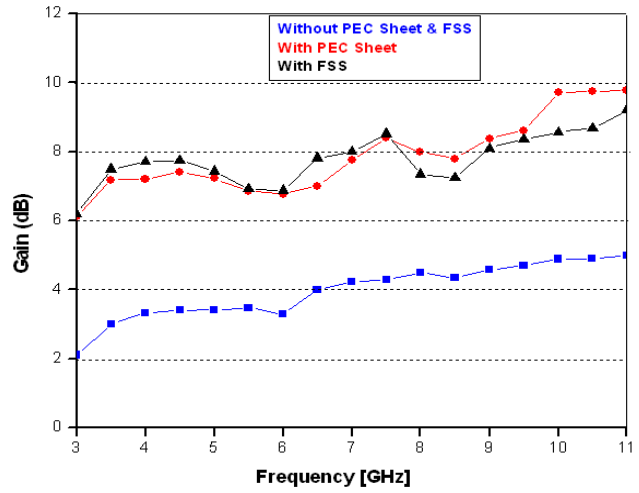
omnidirectional in nature whereas the *H*-plane radiation patterns resemble dumbbell shape. There is a good agreement seen between the measured and simulated radiation patterns for *E* and *H* planes with the slight difference caused by assembly misalignments.

Also, most of the radiation patterns are seem to be reasonably stable with respect to frequency. In the case of antenna without FSS, the *H*-plane pattern shows a pinch-off along the end fire directions ( $\theta = \pm 90^\circ$ ) at lower frequencies, because of the increased cross polarization at these frequency, but when FSS is applied, the pinch-off is no more evident. This shows a reduction in the cross-polar component after the application of the proposed FSS. As shown the *E*-plane pattern, in the case of the antenna with FSS, the pattern becomes more unidirectional in nature, and the back lobes (along  $\theta = 180^\circ$ ) are considerably reduced as expected.

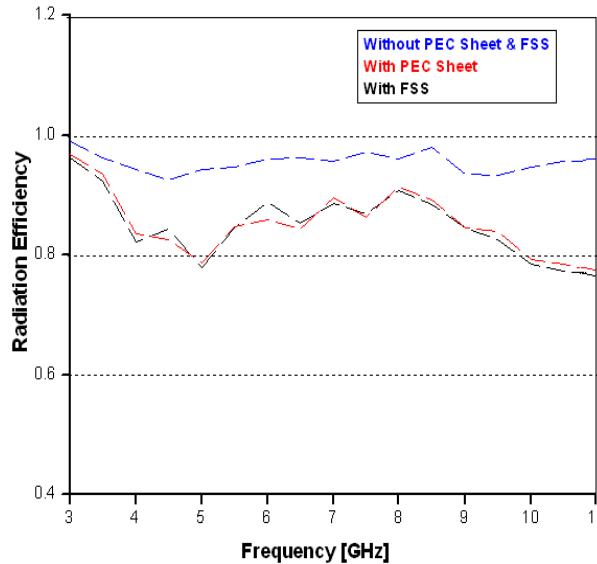




**Figure 33.** Image of structure with PEC sheet (Top view).



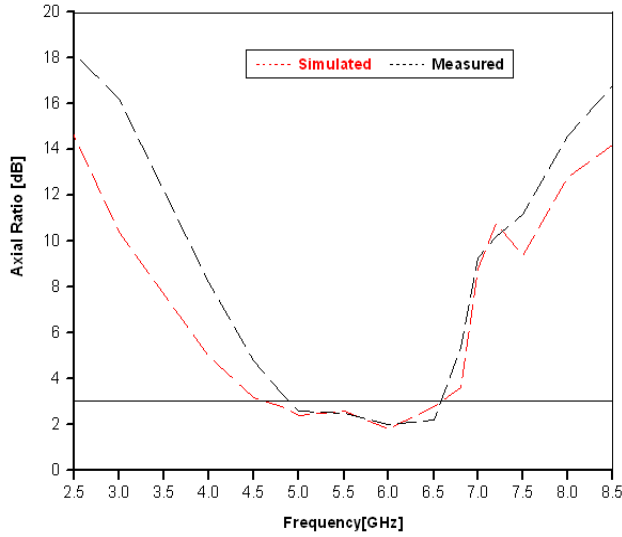
**Figure 34.** Measured peak gains of the proposed antenna without and with the FSS and PEC sheet.



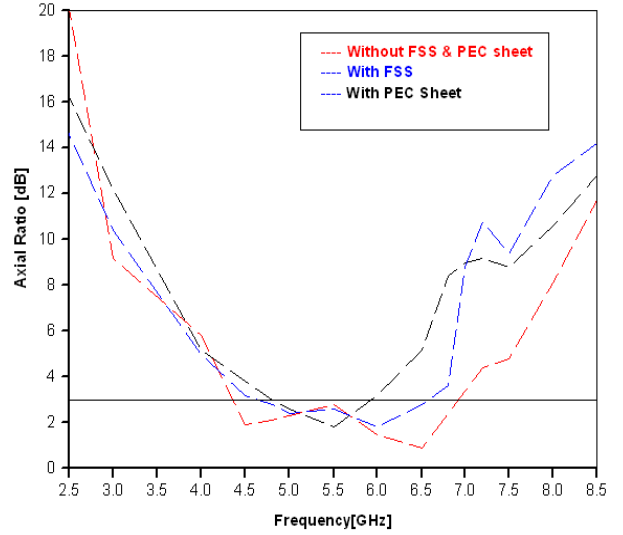
**Figure 35.** Simulated radiation efficiency of the proposed antenna without and with the FSS and PEC sheet.

Figure 33 shows an image of the proposed structure with PEC sheet where the antenna along with the sheet is mounted at optimal height of 20 mm.

A comparison between the measured peak gains (linear, total) for the antenna with and without the FSS and PEC sheet is shown in Figure 34. It shows improvement in gain in the case of antenna with FSS and PEC sheet compared to the antenna without FSS and PEC sheet. The improvement in the gain basically results from an increase in the directivity. From Figure 34, it is observed that on average the improvement in the peak gain is about 4 dB–5 dB. It is also noticed from the figure that the measured gains for all three cases remain low for lower frequency range up to 4.0 GHz. This is due to the poor characteristics (low gain) of the reference horn antenna used in the Antenna Measurement System for this frequency range. The tendency for all the measured gains (with and without FSS and PEC sheet) to increase with increase in the frequency is attributed to the increased aperture area in



**Figure 36.** Simulated and measured axial ratio (along  $\theta = 78^\circ$  and  $\Phi = -89^\circ$ ) of the proposed antenna with the FSS.



**Figure 37.** Simulated and measured axial ratio (along  $\theta = 78^\circ$  and  $\Phi = -89^\circ$ ) of the proposed antenna without and with the FSS and PEC sheet.

higher frequency range (above 9.0 GHz).

The simulated radiation efficiencies of the antenna with and without FSS and PEC sheet are shown in Figure 35. There is approximately a 10–15% reduction in the radiation efficiency in the case of the antenna with FSS and PEC sheet. This reduction is due to the additional losses taking place in the FSS screen or PES sheet and the substrate. It is seen from Figure 35, the radiation efficiency stays above 75% in the operating band.

The CP performance of the proposed antenna is affected in the case with the presence of FSS. It is seen in Figure 36 that the ARBW (axial ratio bandwidth) of the proposed antenna is reduced in the presence of FSS compared to the case without FSS. This effect is due to the phase change in the electric field components induced during reflection from the proposed FSS and interference between the forward traveling and reflected waves. The simulated ARBW is 36% (4.6–6.61 GHz) centered at 5.61 GHz whereas measured ARBW is 27% (4.95–6.51 GHz) centered at 5.73 GHz.

In another case, a PEC sheet is placed as a reflector below the proposed antenna and investigated. In this case, the impedance matching gets affected, and the axial ratio is disturbed by which ARBW (axial ratio bandwidth) is observed to be reduced as shown in Figure 37.

## 6. CONCLUSION

A novel band-reconfigurable octagonal shape monopole antenna with completely switchable frequency bands has been presented. The antenna uses switchable slotted structure on the ground plane to provide band-reconfigurable capability. The proposed antenna is simple to design and uses five p-i-n diodes to switch on the desired frequency bands. The proposed frequency-band reconfigurable antenna is intended for the use in cognitive radio and multi-radio wireless applications.

To improve the gain of the proposed antenna, two frequency selective surface designs are presented. The first is a circular loop FSS designed at the center frequency of 7.51 GHz which provides average improvement in the antenna gain by about 4 dB–5 dB. The second is a PEC sheet type frequency selective surface which, besides enhancing the gain, retains the impedance bandwidth achieved without the frequency selective surface. The measured results seem to be in good agreement with the simulated results.

## REFERENCES

1. Zhang, C., S. Yang, H. K. Pan, A. E. Fathy, and V. K. Nair, "Frequency reconfigurable antennas for multi radio wireless platforms," *IEEE Microwave Magazine*, Vol. 10, No. 1, 66–83, Feb. 2009.
2. FCC (Federal Communications Commission), First Report and Order, Feb. 14, 2002.
3. Li, R. L., T. Wu, S. Y. Eom, S. S. Myoung, K. Lim, J. Laskar, S. I. Jeon, and M. M. Tentzeris, "Switchable quad-band antennas for cognitive radio base station applications," *IEEE Trans. Antennas Propagation*, Vol. 58, No. 5, 1468–1476, May 2010.
4. Mahmoud, S. F. and A. F. Sheta, "A widely tunable compact patch antenna," *IEEE Antennas Wireless Propagation Letter*, Vol. 7, 40–42, 2008.
5. Huang, C. T. and T. Y. Han, "Reconfigurable monopolar patch antenna," *Electron Lett.*, Vol. 46, No. 3, 199–200, Feb. 2010.
6. Gardner, P., M. R. Hamid, P. S. Hall, and F. Ghanem, "Switched-band Vivaldi antenna," *IEEE Trans. Antennas Propagation*, Vol. 59, No. 5, 1472–1480, May 2011.
7. Li, R. L., G. P. Jin, and D. L. Zhang, "Optically controlled reconfigurable antenna for cognitive radio applications," *Electron Lett.*, Vol. 47, No. 17, 948–950, Aug. 2011.
8. Gardner, P., M. R. Hamid, P. S. Hall, and F. Ghanem, "Vivaldi antenna with integrated switchable band pass resonator," *IEEE Trans. Antennas Propagation*, Vol. 59, No. 11, 4008–4015, Nov. 2011.
9. Ghafouri-Shiraz, H. and A. Tariq, "Frequency-reconfigurable monopole antennas," *IEEE Trans. Antennas Propagation*, Vol. 60, No. 1, 44–50, Jan. 2012.
10. Gardner, P., J. R. Kelly, and P. S. Hall, "Integrated wide-narrow band antenna for switched operation," *Processing IEEE EuCAP*, 3757–3760, Berlin, Germany, 2009.
11. Boudaghi, H., M. Azarmanesh, and M. Mehranpour, "A frequency-reconfigurable monopole antenna using switchable slotted ground structure," *IEEE Antennas and Wireless Propagation Letters*, Vol. 11, 2012.
12. Dushmantha, N., P. Thalakituna, L. Matekovits, M. Heimlich, K. P. Esselle, and S. G. Hay, "Active switching devices in a tunable EBG structure: Placement strategies and modeling," *Journal of Electromagnetic Waves and Applications*, Vol. 25, Nos. 11–12, 1740–1751, 2011.
13. Dushmantha, N., P. Thalakituna, K. P. Esselle, L. Matekovits, M. Heimlich, and S. G. Hay, "Changing the electromagnetic bandgap and stopbands in a multistate periodic circuit," *Microwave and Optical Technology Letters (MOTL)*, Vol. 55, No. 8, 1871–1874, Aug. 2013.
14. Kushwaha, N. and R. Kumar, "Design of slotted ground hexagonal microstrip patch antenna and gain improvement with FSS screen," *Progress In Electromagnetics Research B*, Vol. 51, 177–199, 2013.
15. Alpha Industries, "ALPHA-6355 beamlead PIN diode," Data sheet, [Online]. Available: [http://www.datasheetarchive.com/ALPHA/PIN diode 6355-datasheet.html](http://www.datasheetarchive.com/ALPHA/PIN+diode+6355-datasheet.html).
16. Computer Simulation Technology — CST (Microwave Studio MWS), Version-2014.
17. Ray, K. P. and G. Kumar, "Determination of resonant frequency of microstrip antennas," *Microw. Opt. Technol. Lett.*, Vol. 23, 114–117, 1999.
18. Langley, R. J. and E. A. Parker, "Equivalent-circuit model for arrays of square loops," *Electron Lett.*, Vol. 18, 294–296, 1982.
19. Chung, Y.-C., K.-W. Lee, I.-P. Hong, M.-G. Lee, H.-J. Chun, and J.-G. Yook, "Simple prediction of FSS radome transmission characteristics using an FSS equivalent circuit model," *IEICE Electron. Expr.*, Vol. 8, No. 2, 89–95, 2011.
20. Kushwaha, N., R. Kumar, R. V. S. Ram Krishna, and T. Oli, "Design and analysis of new compact UWB frequency selective surface and its equivalent circuit," *Progress In Electromagnetics Research C*, Vol. 46, 31–39, 2014.